Yu, Z.; Huang, Y.; Gan, W.; Mendis, C.L.; Zhong, Z.; Brokmeier, H.-G.; Hort, N.; Meng, J.:

**Microstructure evolution of Mg–11Gd–4.5Y–1Nd–1.5Zn–0.5Zr (wt%) alloy during deformation and its effect on strengthening**

In: Materials Science and Engineering A (2016) Elsevier

DOI: 10.1016/j.msea.2016.01.071

# Microstructure evolution of Mg-11Gd-4.5Y-1Nd-1.5Zn-0.5Zr (wt%) alloy during deformation and its effect on strengthening

Z. Yu[1,2] and Y. Huang[2], W. Gan[2], C. L. Mendis[2], Z. Zhong[2], H. G. Brokmeier[2,3], N. Hort[2], J. Meng[1]

[1]State Key Laboratory of Rare Earth Resources Utilization, Changchun Institute of Applied Chemistry, Chinese Academy of Sciences, Changchun 130022, PR China
[2]Institute of Materials Research, Helmholtz-Zentrum Geesthacht, D-21502 Geesthacht, Germany
[3]Clausthal University of Technology, Institute for Materials Science and Engineering, D38678 Clausthal-Zellerfeld, Germany

## Abstract

Microstructure and texture evolutions during tensile and compression deformation of an as-extruded Mg-11Gd-4.5Y-1Nd-1.5Zn-0.5Zr (wt%) alloy have been investigated using in-situ synchrotron radiation diffraction and subsequent microscopy. The alloy consists of $\langle 10\bar{1}0\rangle$ fiber texture, $\{11\bar{2}0\}[0001]$ and $\{11\bar{2}0\}\langle 10\bar{1}0\rangle$ texture components prior to deformation. The texture evolves from $[0001]$ to $\langle 10\bar{1}0\rangle$ in tension, but from $\langle 10\bar{1}0\rangle$ to $[0001]$ in compression. The evolution of texture is attributed to the activity of the tensile twinning and non-basal $\langle a\rangle$ type slip. The tendency of texture evolution depends on the favorable texture component for the activation of above deformation modes. The grain refinement, $Mg_5$(Gd,Y,Nd) and LPSO phases, and the texture contribute to the improvement in strength.

# 1 Introduction

There is much interest in rare earth (RE) containing Mg alloys due to their outstanding mechanical properties and their potential applications in the automotive and aerospace industries [1]. Compared with the as-cast Mg-RE alloys, the wrought Mg-RE alloys normally have better mechanical properties due to the fine microstructures, uniformly distributed precipitates and weak texture [2–8]. To produce high strength wrought Mg alloys, many investigations on the Mg–Gd based alloys with addition of elements such as Y, Nd, Dy, Zn, Ag etc. have been conducted. Recently, a Mg–10Gd–5.7Y–1.6Zn–0.7Zr (wt%) alloy with a yield strength of 473 MPa and an elongation to failure of 8% was successfully produced by hot extrusion followed by aging [3]. In addition, a Mg–11Gd–4.5Y–1Nd–1.5Zn–0.5Zr (wt%) alloy with a yield strength of 502 MPa and an elongation of 2.6% was also produced by hot extrusion, cold rolling and aging [5,6]. These alloys exhibit a tension– compression asymmetry with a ratio of compressive to tensile yield strength larger than a unity, whereas this value is between 0.3 and 0.7 for most commercial wrought Mg alloys [9]. The reasons for such unusual yield asymmetry were discussed in our previous investigation [10].

Although the attractiveness of wrought Mg alloys with the impressive specific strength (strength/density) could be achieved by various thermomechanical treatments, the limited deformation mechanisms, including dislocation slip and twinning in this low asymmetry hexagonal close-packed (hcp) crystal structure lead to a mechanical response remarkably different from that observed in metals with higher symmetry crystal structures, such as facecentered cubic. Thus, the mechanical properties and deformation behavior of wrought Mg alloys strongly depend on the crystallographic texture $[11\bar{1}2]$. The wrought Mg alloys, which have sharp basal texture, normally exhibit a large anisotropy in both yield strength and ductility [9]. The relationship between texture and deformation modes has been extensively investigated for Mg alloys $[1\bar{1}16]$. The dependence of the active deformation modes on the texture evolution, and vice versa, has been investigated in commercial Mg alloys, such as AZ31 and AM20 [13,15]. The $\{10\bar{1}2\}$ tensile twinning causes a rapid texture change as it leads to a 86.3° rotation of the basal plane [13]. The basal $\langle a\rangle$ slip, which is activated during the initial deformation stage, accounts for the rotation of basal plane parallel to tensile axis [15]. Agnew et al. [12] and Yi et al. [13] suggested the non-basal $\langle a\rangle$ and $\langle c+a\rangle$ slips also contribute to texture variation. More recently, a study on the ultrafine-grained ZK60 alloy revealed that the twinning-induced lattice rotation was favorable for the activation of non-basal $\langle a\rangle$ slip, which assist the texture evolution during deformation [17].

However, it is interesting to note that few intermetallic phase particles were found in the Mg alloys investigated above. In contrast, many intermetallic phase

particles are observed in the high strength wrought Mg-RE alloys due to the high concentration of RE addition. Only limited studies on the texture evolution and deformation behavior have been conducted on such Mg-RE alloys [18]. To improve strength, ductility and workability of high strength wrought Mg-RE alloys, the relationship between active deformation modes and texture evolution during deformation needs to be further investigated. The previous investigations on Mg-RE-Zn alloys show that the LPSO phase, which forms parallel to the extrusion direction (ED), significantly improves the mechanical properties via the short-fiber strengthening mechanism [19,20]. Hagihara et al. [21] suggested that the $(0001)\langle 11\bar{2}0\rangle$ basal slip is the dominant operative deformation mode in LPSO phase, so that the deformation behavior of the LPSO phase shows a strong anisotropy depending on the loading direction. Therefore, the LPSO phase containing Mg alloys (Mg-LPSO phases) are highly sensitive to the loading direction from the perspective of the deformation behavior and mechanical properties [19]. Although the role of LPSO phase plays on the mechanical properties and deformation behavior has been extensively investigated [19,22], there is very little information in the literature on its influence evolution of microstructure and texture during deformation.

In this paper, we aim to report the findings from an investigation on the changes in microstructure and texture evolution of a Mg–11Gd–4.5Y–1Nd–1.5Zn–0.5Zr (wt%) alloy during uniaxial tension and compression, and to clarify the relationships between texture evolution, active deformation modes and mechanical properties. Since texture has a large impact on the selection of the active deformation modes, the accurate measurement of the changes in individual deformation modes, which accompany texture evolution, is exceedingly difficult to be performed. For this reason we used in-situ synchrotron radiation to examine the deformation behavior and texture evolution during deformation.

# 2 Experimental Procedures

## 2.1 Materials and Processing

Mg–11Gd–4.5Y–1.5Zn–1Nd–0.5Zr (wt%) cylindrical billet was prepared by pouring melt into a cylindrical steel mould with a diameter of 92 mm at 760 $\pm$ 3 °C under a mixture of $SF_6/CO_2$ (1:99) protective atmosphere. The mould was preheated to 200 $\pm$ 3 °C prior to the casting. The billet was homogenized at 535 $\pm$ 3 °C for 24 h and quenched into water (25 °C). The homogenized billet was machined into a round bar with a diameter of Ø 82 mm x 120 mm for subsequent hot extrusion at 410 $\pm$ 3 °C with an extrusion ratio of 30:1. A pre-aging treatment

was conducted at 410 $\pm$ 3 °C for 1 h before hot extrusion. The extruded sample was designated as ER30.

## 2.2 Microstructure Observations

The microstructures were observed with optical microscopy (OM) using a Leica DMI 5000 light optical microscope, scanning electron microscopy (SEM) using Zeiss Ultra 55 SEM equipped with an TSL electron back scattered diffraction (EBSD) operating at 15 kV, and transmission electron microscopy (TEM) using Philips CM 200 TEM operating at 200 kV. The samples for OM and SEM observations were ground with SiC papers to 2500 grit and polished with 0.05 $\mu$m OP-S suspensions. The TEM samples were ground with SiC papers to a thickness of 120 mm and then electro-polished to perforation (2.5 vol% perchloric acid and 97.5 vol% ethanol, at 47 °C, 40 V) using a Fishionie twin-jet electropolisher.

X-ray diffraction (XRD) measurements for phase analysis were performed using a laboratory X-ray diffractometer (Siemens D5000, 40 kV and 40 mA) with Cu K$\alpha$ radiation and with a secondary monochromatic beam (scan range 10–90°, step size 0.03° $s^{-1}$, dwell time 3 s). The average size of grains was measured using liner intercept method.

## 2.3 Texture characterization

The in-situ texture measurements were conducted using high energy X-rays (87 keV) with a wavelength of 0.0142 nm and an incident beam size of 200 x 200 $\mu m^2$ at the High Energy Material Science (HEMS) of Helmholtz-Zentrum Geesthacht Beamline experimental station P07B at PETRA III storage ring, at DESY (Deutsches Elektronen Synchrotron) Germany [23]. The tensile and compression tests were conducted with the plate tensile specimens and cylindrical compression specimens (gauge dimension: 20 mm x 4mm x 2 mm and Ø 11 mm x 16.5 mm) along the ED with a speed of 1 mm $min^{-1}$ using a universal testing machine.

Three specimens were tested in order to obtain the average value and standard deviation. The tensile and compression tests were conducted in-situ using synchrotron radiation using a separate sample geometry [24]. One specimen was tested for each condition as the mechanical properties obtained with in-situ test were comparable to the testing done ex-situ.

The in-situ texture measurement points were selected on the stress–strain curves corresponding to the typical points: before loading, before and after yielding, during strain hardening and at quasi-steady plastic deformation and after fracture. The loading was stopped but not released at each point where the pole figures were measured, and then the sample was rotated by 120° with a step size of 5° and was irradiated for 0.1 s at each step.

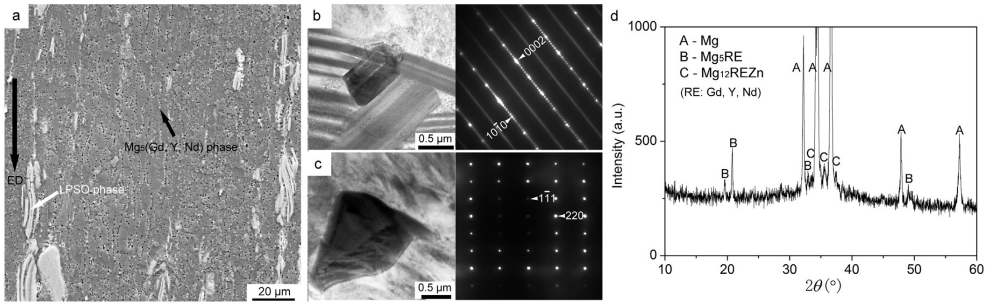


Figure 1: (a) SEM image of the sample ER30; TEM images and SAED patterns of (b) LPSO phase ($B\|[1120]\alpha$-Mg) and (c) $Mg_5$(Gd,Y,Nd) particles ($B\|[112]$ $Mg_5$(Gd,Y,Nd)); (d) XRD patterns of sample ER30. Note that B is the incident electron beam.

Five pole figures, $\{10\bar{1}0\}$, $\{0002\}$, $\{10\bar{1}1\}$, $\{10\bar{1}2\}$ and $\{11\bar{2}0\}$ were calculated at each point with respective Debye-Scherrer rings recorded using a PE 1621 flat panel area detector. The harmonic iterative series expansion method was employed for the calculation of orientation distribution function (ODF) using these five incomplete pole figures. The inverse pole figures were recalculated after the ODF calculation. The SEM-EBSD measurements (15 keV, step size 0.2 $\mu$m) were used to analyze the local microstructures and textures.

# 3 Results

## 3.1 Microstructure Characterizaton

The microstructure of sample ER30 is shown in Fig. 1a. After extrusion, the sample ER30 exhibits a typical microstructure of fine dynamic recrystallized (DRXed) grains. The average grain size is 3.6 $\pm$ 1.3 $\mu$m. It can also be seen that the microstructure contains LPSO phase (white arrow) and bulk phase (black arrow). The rodlike LPSO phase particles distribute along ED, and the bulk phase particles are located at grain boundaries. The TEM image (Fig. 1b) shows the LPSO phase particles in the sample ER30. The selected area electron diffraction (SAED) pattern recorded from the LPSO phase indicates that this phase has a 14H-type structure. A typical bulk phase particle and corresponding SAED pattern are shown in Fig. 1c. The SAED pattern indicates that this granular phase has a cubic structure. The XRD measurement was conducted to further analyze the second phases in the sample ER30. As a result, $Mg_5$(Gd,Y,Nd) and $Mg_{12}$(Gd,Y,Nd)Zn phases can be identified in XRD pattern (Fig. 1d). According to the previous studies, the bulk phase can be indexed as Mg5(Gd,Y,Nd) phase (F4$\bar{3}$m, a = 2.2 nm) [25].

| Test | in-situ | | | ex-situ | | |
|---|---|---|---|---|---|---|
| tension | 320 | 388 | 7.8 | 309 ± 1.0 | 363 ± 3.2 | 6.2 ± 0.9 |
| compression | 372 | 520 | 12.8 | 363 ± 1.4 | 540 ± 4.4 | 10.5 ± 0.2 |

Table 1: Mechanical properties of ER30 alloys obtained during compression and tensile testing performed in-situ and ex-situ synchrotron radiation diffraction.

The orientation relationship between $Mg_5$(Gd,Y,Nd) phase and $\alpha$-Mg matrix is (110)$Mg_5$(Gd Y,Nd)//(0001)$\alpha$-Mg, $[11\bar{1}]Mg_5$(Gd,Y,Nd)//$[2110]\alpha$-Mg. The 14H-type LPSO phase can be indexed as $Mg_{12}$(Gd,Y,Nd)Zn phase [26]. The composition of these phases was investigated in our previous study, see reference [10].

## 3.2 Mechanical Properties

The tensile and compressive properties measured with the insitu and the ex-situ setups are summarized in Table 1. The mechanical properties recorded for both in-situ and ex-situ tests are very similar, and summarized the tensile and compressive properties based on the ex-situ results as follows:

1. The sample ER30 has an ultimate tensile strength ($\sigma_{UTS}$) of 363 $\pm$ 3.2 MPa, a 0.2% proof stress ($\sigma_{TPS}$) of 306 $\pm$ 1.0 MPa and an elongation to failure of 6.2 $\pm$ 0.9%.

2. The sample ER30 has a higher ultimate compressive strength ($\sigma_{UCS}$) of 540 $\pm$ 4.4 MPa, a 0.2% proof stress ($\sigma_{CPS}$) of 363 $\pm$ 1.4 MPa and an elongation to failure of 10.5 $\pm$ 0.2% compared with the tensile mechanical properties.

3. The calculated yield strength asymmetry with the ratio between compressive to tensile is greater than unity, at 1.2.

## 3.3 In-situ synchrotron radiation during tensile and compressive deformation

The in-situ synchrotron radiation experiments were used to examine the texture evolution during tensile and compressive deformation for the sample ER30. The stress–strain curves recorded during in-situ measurements are shown in Fig. 2. Several texture measurement points were selected at typical stages on the curves for the characterization of texture evolution. The texture evolution for each sample is presented as pole figure (PF) and inverse pole figure (IPF).

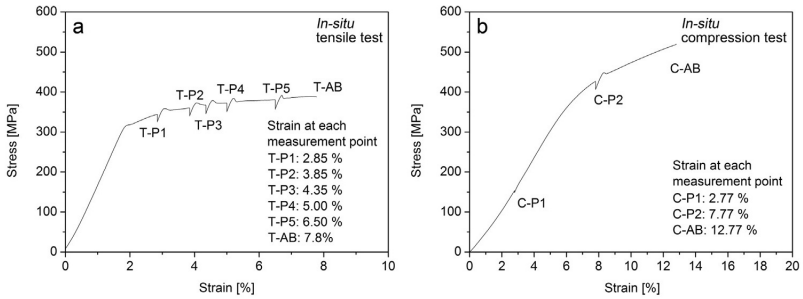


Figure 2: In-situ stress-strain curves of the samples ER30 during (a) tensile test and (b) compression test.

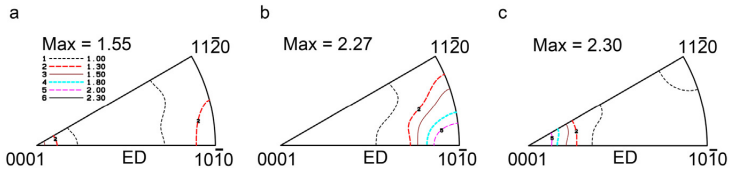


Figure 3: IPF of the sample ER30 at various measurement points: (a) initial, (b) T-AB and (c) C-AB.

### 3.3.1 Texture prior to deformation

The IPF in Fig. 3a shows the initial texture which is not typical of alloys containing RE elements in which the texture peak spreads towards $\langle 11\bar{2}1\rangle$. Two strong texture peaks are located at the arcs of $[0001]$ and $\langle 10\bar{1}0\rangle$ in the IPF are observed in this case. It is evident from the $(0001)$ and $\{10\bar{1}0\}$ pole figures in Fig. 4 that the sample ER30 has an initial texture with $\langle 10\bar{1}0\rangle$ fiber component before testing. The orientation girdle of the $\langle 10\bar{1}10\rangle$ fiber component shows various intensities in the $(0001)$ pole figure, in which a pair of stronger intensity peaks (black dashed circles) spread toward the transverse direction (TD). This indicates that an extra texture component forms in this sample, and is identified as $\{11\bar{2}0\}\langle 10\bar{1}0\rangle$ texture component according to the $\{10\bar{1}10\}$ pole figure (black dashed circles). Additionally, a weak $\{11\bar{2}0\}[0001]$ texture component, which is highlighted by green dashed circles in $(0001)$ and $\{10\bar{1}0\}$ pole figures, is also observed in this sample. The $[0001]$ texture in the IPF corresponds to the $\{11\bar{2}0\}[0001]$ texture component in PF, and the $\langle 10\bar{1}0\rangle$ texture in the IPF corresponds to the $\langle 10\bar{1}0\rangle$ fiber component and $\{11\bar{2}0\}\langle 10\bar{1}0\rangle$ texture component in PF.

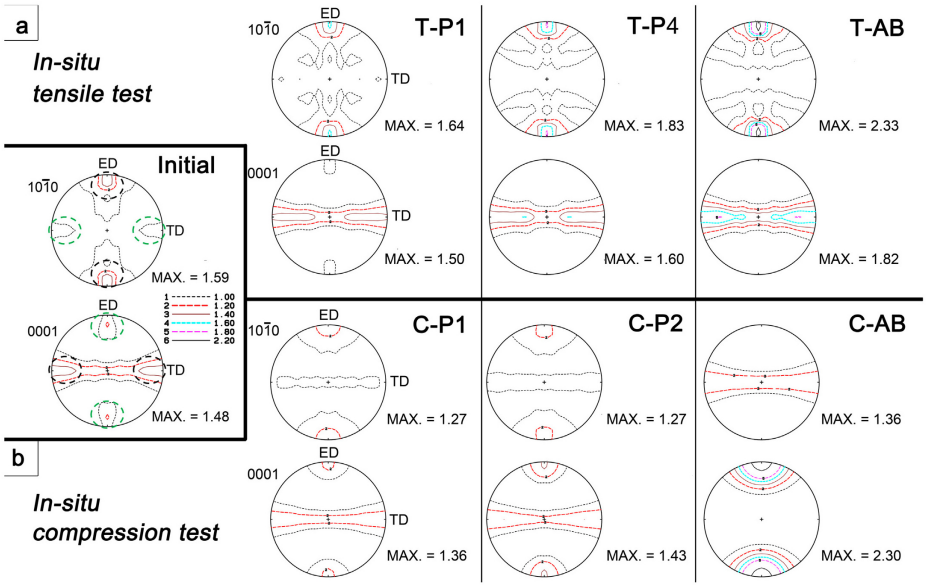


Figure 4: PF of the sample ER30 at various measurement points during in-situ (a) tensile test and (b) compression test.

### 3.3.2 In-situ texture evolution during deformation

The IPFs show that the texture of the alloy consists of unique component at the arc of $\langle 10\bar{1}0\rangle$ after tensile test (Fig. 3b) and at the arc of $[0001]$ after compression test (Fig. 3c). Fig. 4a shows the texture evolution during tensile deformation for the sample ER30 as PFs. The $\{11\bar{2}0\}[0001]$ texture component disappeared during plastic deformation in the quasi-steady state (T-P4), while $\langle 10\bar{1}0\rangle$ fiber component and $\{1120\}\langle 10\bar{1}0\rangle$ texture component gradually strengthened. Finally, the texture comprises $\langle 10\bar{1}0\rangle$ fiber component and $\{11\bar{2}0\}\langle 10\bar{1}0\rangle$ texture component at the end of the test. The maximum intensity increased with the increase in tensile strain and eventually reached to 2.33 multiple of random distribution (M.R.D). In contrast, the PFs reveal that the texture evolution during compressive deformation is opposite to that observed during tensile deformation, Fig. 4b. The $\{11\bar{2}0\}[0001]$ texture component was strengthened with increased compressive strain, while the $\langle 10\bar{1}0\rangle$ fiber component and $\{11\bar{2}0\}\langle 10\bar{1}0\rangle$ component were gradually weakened and eventually disappeared at the end of the test. As a result, the texture consisted of a $[0001]$ fiber texture with a maximum intensity of 2.30 M.R.D.

The intensity variation for individual texture components was analyzed using orientation distribution function (ODF) (Fig. 5). During tensile deformation, the prominent changes are the strengthening of $(0001)[1010]$, $(1213)[1010]$ and $(1210)[1010]$ (components B, C and D) and the weakening of $(1210)[0001]$,

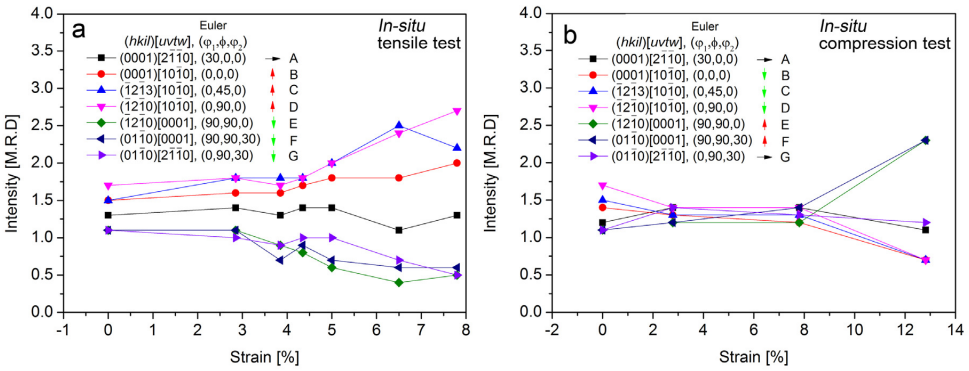


Figure 5: Intensity variation of main texture components for the sample ER30 measured with synchrotron radiation diffraction during in-situ (a) tensile test and (b) compression test.

$(1010)[0001]$ and $(1010)[2110]$ (components E, F and G). There is no significant change for the texture component $(0001)[2110]$ (component A). It is interesting to note that the intensity of the component D increased while that of the component E reduced, even though both components have $(1210)$ plane parallel to the ED. The difference between the components D and E is that the $(1010)$ plane of component D is perpendicular to the ED, while $(0001)$ plane of component E is perpendicular to the ED. The aforementioned texture changes began at the position T-P3, at a corresponding tensile strain of 4.35% (Fig. 5a). During compressive deformation, the intensity of the texture components B, C and D continued to decrease and became lower than unity, while that of the components E and F continually increased (Fig. 5b) during deformation. The components A and G have a negligible change. The texture evolved from the beginning of the testing.

## 3.4 Microstructure evolution during tensile and compressive deformation

Fig. 6a and b shows the EBSD-CI maps of the sample ER30 at T-P2 on the tensile flow curve and C-AB on the compressive flow curve. In the EBSD-CI maps, the small black spots and large black regions are $Mg_5$(Gd,Y,Nd) phase particles and LPSO phase particles, respectively. The grain boundaries were outlined by black lines. Moreover, the $\{11\bar{2}0\}\langle 10\bar{1}1\rangle$ tensile twin (T-twin), $\{10\bar{1}1\}\langle 11\bar{2}0\rangle$ compressive twin (C-twin) and $\{10\bar{1}1\} - \{11\bar{2}0\}$ secondary twin (S-twin) were identified through their misorientation angles from the untwinned regions, which are 86° for T-twin, 56° for C-twin and 38° for S-twin, respectively (Note that only the $\{10\bar{1}1\} - \{11\bar{2}0\}$ secondary twin can be detected among a number of

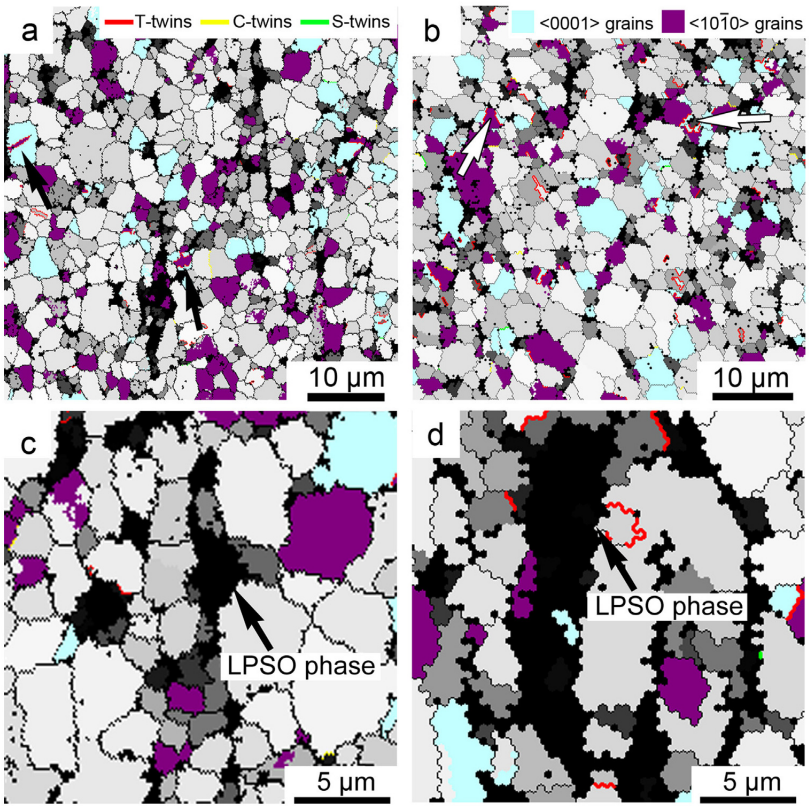


Figure 6: EBSD-CI map of the sample ER30 at measurement points (a and c) T-P2 and (b and d) C-AB.

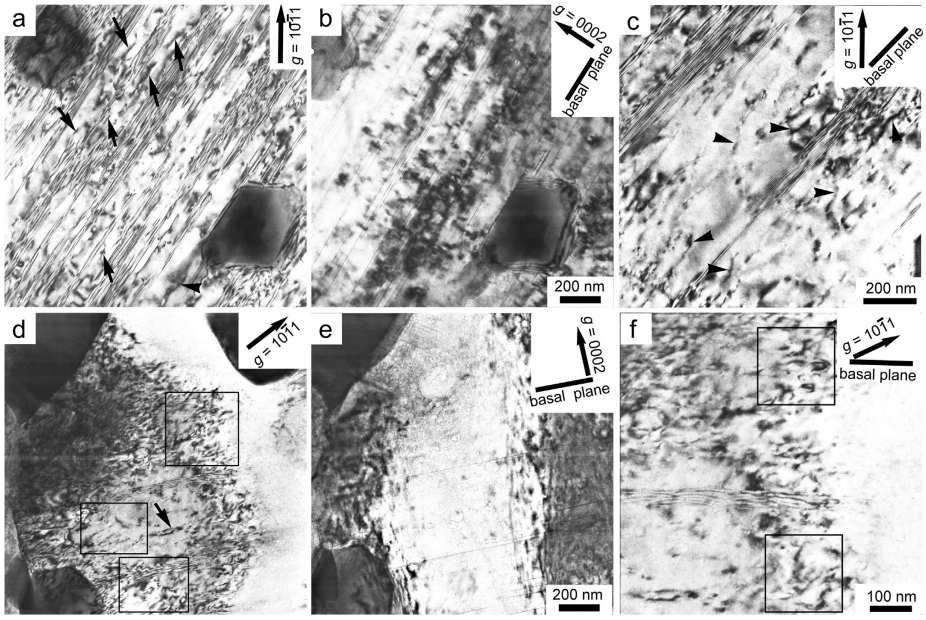


Figure 7: TEM-BF images of the sample ER30 at (a, b and c) T-P2 and (d, e and f) T-AB in two-beam condition with $g = [0001]$ and $g = [1010]$. Note that g is the symbol of operating vector.

secondary twins). At the point T-P2 the number fraction of various twins was approximately 1.6% for T-twin, 0.3% for C-twin and 0.3% for S-twin (Table 2). At the point C-AB the number fraction of T-twin increased to 4.6%, while this value for both C-twin and S-twins show a negligible change. In contrast, these values in ER30 (prior to testing) are only 0.5% for T-twin, 0.3% for C-twin and 0.4% for S-twin. The Fig. 4 shows that the initial texture evolved into $\langle 1010 \rangle$ fiber texture and $\{1120\}\langle 1010 \rangle$ texture after tensile deformation and into $[0001]$ fiber texture after compression deformation. To investigate the effect of twinning on the texture evolution, the $[0001]$ and $\langle 1010 \rangle$ grains were highlighted in light blue and purple (Fig. 6a and b). The $\langle 1010 \rangle$ grains nucleated at T-twins (black arrows) in the $[0001]$ grains during tensile deformation. The $\langle 1010 \rangle$ grains tended to consume the $[0001]$ grains with the growth of T-twins as shown in Fig. 6a. In contrast, the $\langle 1010 \rangle$ grains were gradually consumed by the growth of T-twins, where the $[0001]$ grains nucleated (white arrows) during compressive deformation as shown in Fig. 6b. Fig. 6c and d shows the typical LPSO phase particles and the nearby grains at the points T-P2 and C-AB. The $\langle 1010 \rangle$ and $[0001]$ grains rarely formed around these LPSO phase particles, nor did the T-twins. This indicates that the LPSO phase has an effect on the transition of the $\langle 1010 \rangle$ and $[0001]$ grains by activating the T-twins.

The bright field (BF) TEM micrographs show that this alloy has a large number of stacking faults (SFs) inside the grains after tensile deformation (Fig. 7). In the sample at point T-P2, a large number of dislocations (black arrows) were observed in the regions, in which the SFs are densely distributed on the basal plane (Fig. 7a). These dislocations are identified as $b = 1/3[11\bar{2}0]$ and $b = 1/3[\bar{2}110]$ ($\langle a \rangle$) due their visibility for $g = [10\bar{1}1]$ (e.g. Fig. 7a) and invisibility for $g = [0002]$ (e.g. Fig. 7b). No dislocations are visible simultaneously in Fig. 7a and b, indicating that the $\langle c \rangle$ type and $\langle c + a \rangle$ type slips were not activated at the early stage of tensile deformation. The majority of the observed dislocations can be identified as basal dislocations due to their straight appearance on the basal plane in Fig. 7a–c. The basal slip tended to dominate at the early stage of tensile deformation. In addition, several dislocations (black arrowheads) appear curved, indicating that they are gliding on non-basal planes (Fig. 7a and c). However, their limited amount demonstrates that they were not the dominant deformation mechanism at T-P2. In the fractured sample, the Burgers vectors of the observed dislocations can be defined as $\langle a \rangle$ type on the basis of the $g * b$ criterion, while $\langle c \rangle$ type and $\langle c + a \rangle$ type dislocations were not observed (Fig. 7d and e). Note that the majority of the $\langle a \rangle$ type dislocations appear strongly curved or entire loops as highlighted in the squares in Fig. 7d and f. Only few dislocations remain on the basal planes (black arrow). It is evident that the non-basal $\langle a \rangle$ type slip was the dominant mode of deformation.

The TEM micrographs in Fig. 8 show the microstructures at the points C-P2 and C-AB. In comparison with the microstructure at T-P2, a large number of non-basal dislocations (black arrow) were activated in the $\alpha$-Mg matrix at C-P2, Fig. 8a. The movement of dislocations on the basal plane by slip (white arrow) was also observed here. Additionally, the dislocation walls form by the assembly of a set of parallel dislocations was observed in Fig. 8b. Thus, the grain had subdivided into small cells. In addition to the basal (white arrows) and non-basal slip (black arrows) dislocations, the cross slip (black arrowheads) from basal plane to non-basal plane were activated at C-AB, Fig. 8c. The interactions between the moving dislocations resulted in dislocations tangles, which limit further motion of dislocations. In addition, the nonbasal dislocations can be bound by basal SFs, thus, preventing the movement of non-basal dislocations (white arrowheads). These dislocations were visible with $g = [10\bar{1}1]$, Fig. 8c, but invisible with $g = [0002]$, Fig. 8d, are $\langle a \rangle$ type dislocations with $b = 1/3[11\bar{2}0]$ and/or $1/3[\bar{2}110]$.

In Fig. 9a the sub-grains, marked as A1 and A2, were observed to nucleate near the $Mg_5$(Gd,Y,Nd) particle in the fractured sample after tensile test. These sub-grains tended to spread through the deformation zones inside the grain. The sub-grain boundaries appeared in the same grain as indicated by black arrows in Fig. 9b. These sub-grain boundaries traversed through the whole grain and subdivided it into small cells. Similarly, the sub-grains, marked as B1 and B2,

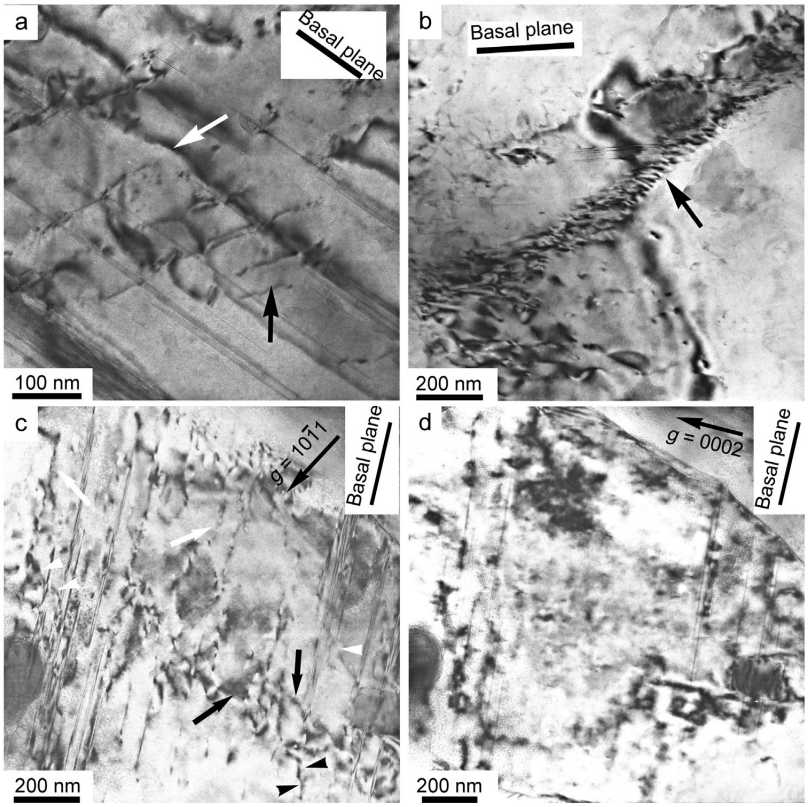


Figure 8: TEM-BF images of the sample ER30 at (a and b) C-P2 and (c and d) C-AB. (c and d) Images are obtained in two-beam condition with $g = [0001]$ and $g = [1010]$.

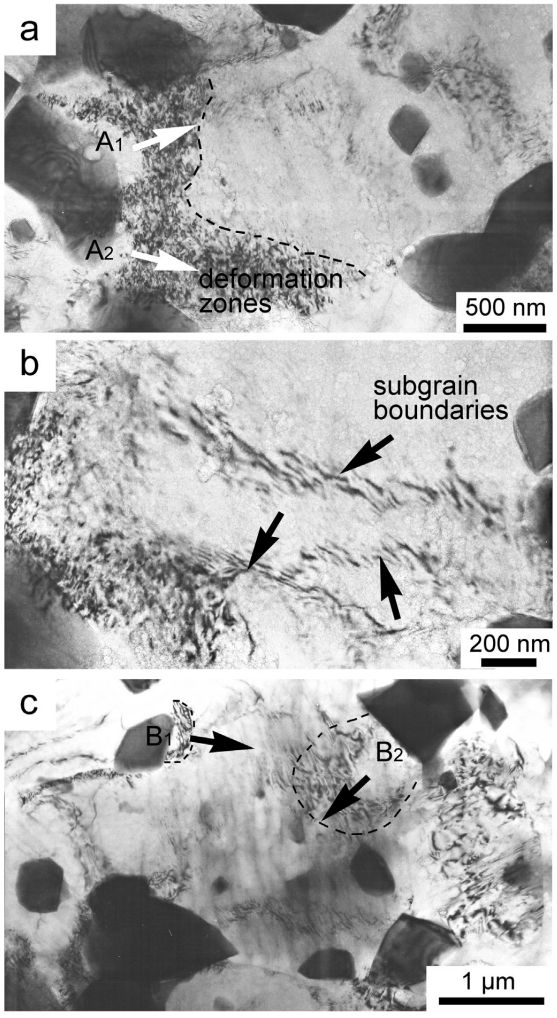


Figure 9: TEM-BF images of the sample ER30 at (a and b) T-AB and (c) C-AB.

also nucleated at the $Mg_5$(Gd,Y,Nd) particles and spread towards grain interior after compression test (Fig. 9c).

# 4 Discussion

## 4.1 Texture evolution and deformation behavior during tension and compression

### 4.1.1 Role of tensile twins

The texture evolution in the sample ER30 during tensile and compression tests are shown in Figs. 4 and 5. In tension the texture evolved from $[0001]$ to $\langle 1010 \rangle$, the most prominent texture change was the disappearance of $[0001]$ texture components E and F and the strengthening of $\langle 1010 \rangle$ texture components B, C and D. In compression the texture evolved from $\langle 1010 \rangle$ to $[0001]$, here the $\langle 1010 \rangle$ texture components B, C and D decreased and eventually disappeared, while the $[0001]$ texture components E and F were continuously strengthened. This type of texture development was always attributed to the high activity of tensile twinning during the initial stage of deformation. Firstly, the $[0001]$ texture with basal planes perpendicular to the ED is in an orientation favorable for tensile twinning when in tension, and the $\langle 1010 \rangle$ texture is favorable for tensile twinning when in compression. Secondly, the 86° lattice rotation by tensile twinning rapidly rotates the c-axis from being parallel to the ED to normal or vice versa [13,15]. Although some of the $\langle 1010 \rangle$ grains form by the consumption of $[0001]$ grains due to tensile twinning (Fig. 6a), this alloy shows low twinning activity at the measurement point T-P2, at which the number fraction of tensile twin is 1.6%. Similarly, some of the $\langle 1010 \rangle$ grains are consumed by the $[0001]$ grains due to tensile twinning in compression, however, the number faction of T-twin is low, and is only 4.6% at C-AB (Fig. 6b). The limited twinning activity is due to the grain refinement and dense distribution of SFs [9,27,28]. Although the twinning activity is limited, the tensile twinning could still contribute to the texture evolution from $[0001]$ to $\langle 1010 \rangle$ or vice versa, especially in this alloy where there is a weak initial texture. This result is different from that obtained for the extruded AZ31 and AM20 alloys, in which the high activity of tensile twinning is the main factor for the rapid change of texture [13,14]. Therefore, there should be some other factors to influence such texture evolution.

### 4.1.2 Role of dislocations

During tension the plastic deformation begins with basal $\langle a \rangle$ slip, even with its low Schmid factor as the initial texture components having the basal plane parallel or

perpendicular to the tensile direction. Therefore, a relatively high yield stress is achieved, and this stress reaches high enough for the activation of non-basal $\langle a \rangle$ slip soon after yielding (Fig. 7c). As aforementioned that the T-twins form by the consumption of $[0001]$ texture component, and such variation in texture is favorable for the basal $\langle a \rangle$ slip after twinning [13]. However, the low twinning activity and the dominance of basal $\langle a \rangle$ slip result in subtle texture changes, in which the $[0001]$ texture components E and F begin to slightly reduce at T-P1, while the $\langle 1010 \rangle$ texture components B, C and D remain nearly unchanged until the non-basal $\langle a \rangle$ slip become dominant at measurement T-P3. It is unlikely that the basal $\langle a \rangle$ slip is the factor contributing to the texture evolution from $[0001]$ to $\langle 1010 \rangle$.

In tension, the strengthening of one texture component is accompanied by the weakening of other texture components, such that the intensity of the texture component $(1210)[1010]$ (D) increased while that of components $(1210)[0001]$ (E) and component $(1010)[1210]$ (G) decreased (Fig. 5a). The development of texture component $(1210)[1010]$ (D) is attributed to the weakening of component $(1010)[1210]$ (G), as the basal planes of both components are parallel to the ED and the 30° rotation of these two components can be satisfied by combination of basal and nonbasal $\langle a \rangle$ slip [14]. Although the components D and E have $(1210)$ planes parallel to the ED, they differ from each other as the c-axis of the component E is parallel to ED, while the c-axis of the component D is perpendicular to ED. This relation reveals that the rapid and large texture change from the component E to component D cannot be achieved by slip but by tensile twinning for two reasons. Firstly, the component E is unfavorable for basal slip but favorable for T-twin. Secondly, the tensile twinning provides an approximately 86° rotation of basal plane, so that the activation of T-twin satisfied the texture evolution from component E–D. Another texture change is the strengthening of the component $(1213)[1010]$ (C) (Fig. 5a). The previous investigation suggested that strengthening of this component was attributed to the continuous non-basal $\langle a \rangle$ slip [13,14]. Since the non-basal $\langle a \rangle$ slip was activated soon after yielding, the component C was slightly strengthened at T-P1 and remarkably strengthened from T-P3. The dominant deformation mode shifted to non-basal $\langle a \rangle$ slip, which accommodated the majority of deformation until fracture. The shift in the texture component from $[0001]$ to $\langle 1010 \rangle$ can be attributed to the combined contribution of tensile twinning and non-basal $\langle a \rangle$ slip.

In compression, the non-basal dislocations dominated the compressive deformation at C-P2. The dislocation walls were formed by assembly of the parallel basal dislocations to accommodate the plastic deformation. These dislocations were identified as $\langle a \rangle$ type dislocations in the Fig. 8c and d, which illustrate the microstructures at the point C-AB in two-beam condition. In contrast to the texture evolution in tension, the texture evolved from$\langle 1010 \rangle$ to $[0001]$ from the beginning

of compression. It is evident that the strengthening of $[0001]$ texture components E and F is accompanied by the weakening of $\langle 1010 \rangle$ texture component B, C and D. The difference in texture evolution at initial tensile and compressive deformations is attributed to the fact that the alloy has strong $\langle 1010 \rangle$ texture, which is favorable for tensile twinning in compression, but weak $[0001]$ texture, which is favorable for tensile twinning in tension. Thus, the texture evolution responses relatively stronger at the beginning of compression compared to that at the beginning of tension. However, the texture change was not significant until C-P2. From the texture perspective, neither [0001] nor $\langle 1010 \rangle$ textures are favorable for the basal $\langle a \rangle$ slip in compression. Even though the $\langle 1010 \rangle$ texture is favorable for tensile twinning, but the activation of T-twins was still limited as the number fraction of T-twin was only 4.6% at C-AB. Thus, the limited texture change is due to the low activation of tensile twinning during the initial stage of compression. With the increase in compressive strain, the texture component evolved into $[0001]$ texture by the consumption of $\langle 1010 \rangle$ texture after C-P2. However, the contribution of T-twin is not high enough to cause the evolution of $[0001]$ texture. The non-basal $\langle a \rangle$ slip should be involved in the further evolution of texture. The non-basal $\langle a \rangle$ slip begins to dominate the deformation at C-P2 (Fig. 8a and b), which is consistent with critical change of texture from $[0001]$ to $\langle 1010 \rangle$ (Fig. 4b). Thus, the texture evolution relates mainly to the combination of T-twin and non-basal $\langle a \rangle$ slips. It is evident that the texture evolution depends on the main deformation modes in tension and compression, inversely, the change in the main deformation modes, from basal $\langle a \rangle$ slip and tensile twinning to nonbasal $\langle a \rangle$ slip, in?uence on the texture evolution. The tendency of texture evolution depends on the favorable texture component for the activation of main deformation modes.

### 4.1.3 Role of second phase particles

A large number of LPSO phase particles and $Mg_5$(Gd,Y,Nd) phase particles are located at the grain boundaries in the sample ER30, and their role on the texture evolution should not be neglected. After tension and compression, the $[0001]$ and $\langle 1010 \rangle$ grains rarely form in the vicinity of the LPSO phase particles (Fig. 6c and d). Hagihara et al. [19,21] suggested that the $(0001)\langle 11\bar{2}0 \rangle$ basal slip is the dominant deformation mode in the LPSO phase at room temperature. The uniformly distributed LPSO phase particles have the $(0001)$ LPSO parallel to the ED, where is unfavorable for the activation of basal slip both in tension and compression. The LPSO phase particles act as a skeleton, which can withstand large external loads and prevent the nearby grains from rotation. The coherent interface between LPSO phase and Mg grain are not favorable for nucleation of defects during deformation [27]. Thus, the difficulties in the rotation of the nearby grains and in the

nucleation of defects at Mg/LPSO interfaces indicate that the LPSO phase could effectively hinders the texture evolution.

In addition to the LPSO phase particles, $Mg_5$(Gd,Y,Nd) particles can also pin the movement of grain boundaries. This may explain the minor texture changes at the initial deformation stage in tension and compression. With further deformation, a large deformation zone forms near the $Mg_5$(Gd,Y,Nd) particles and occupy 1/3 area of whole grains (Fig. 9a). Similarly, the deformation zone was also found at these particles following compression (Fig. 9c). The large deformation gradient induced by these particles cause the deformation zone to progressively rotate away from its original orientation. The final orientation of the deformation zone is related to the activation of slip systems, as a large number of dislocations are needed to produce the required rotation where twinning activity is low [29]. Two nuclei A1 and A2 form at the particle and tended to propagate towards the grain interior by the consumption of the deformation zones in tension (Fig. 9a). Similar, the nuclei B1 and B2 at the particle tended to propagate towards grain interior in compression. The driving force is the reduction in dislocation density and boundary energy [29]. The initial stage of recrystallization takes place through PSN (particles simulated nucleation) at room temperature during tensile and compressive deformation. The growth of these nuclei would make the deformation zone incompatible with the deformed matrix. This contributed to the texture development during tensile and compressive deformation.

## 4.2 Role of microstructure in strengthening

The mechanical properties of the extruded alloy are summarized in Table 1. The microstructural features described above contributes to the improvement of mechanical properties for the investigated alloy. The average grain size of DRXed grains for the sample ER30 is only 3.6 $\pm$ 1.3 $\mu$m, which leads to a high yield strength based on the Hall–Petch strengthening.

The typical texture observed another factor that contributes to the strength of the alloy. The sample ER30 consists of $[0001]$ and $\langle 1010 \rangle$ textures parallel to the ED. The in-situ measurements show a change in texture, such that the $[0001]$ grains reoriented their caxis perpendicular to ED. This $[0001]$ texture assists the tensile twinning when the tensile direction is parallel to the ED. The Fig. 6 shows tensile twinning initiates in the $[0001]$ grains and created a $\langle 1010 \rangle$ grains inside the twined region by a consumption of $[0001]$ grains. The activation of twinning decrease the yield strength, however, tensile twins were less pronounced due to the grain refinement and the dense distribution of SFs [9,27,28]. Thus, other factors should be responsible for the textural evolution and mechanical properties.

The basal $\langle a \rangle$ slip accommodates the stress concentration and is the dominant deformation mechanism at the initial stage of tensile deformation, even with a

negligible Schmid factor, for the activation of this deformation mode, in relation to the initial texture, which has the $[0001]$ and $\langle 1010\rangle$ orientations parallel to the ED. Therefore, a high yield stress is achieved since the majority of grains have their basal planes parallel or perpendicular to the loading direction. The $\langle 1010\rangle$ texture components B, C and D remain nearly unchanged until T-P3, indicating that the basal $\langle a\rangle$ slip is still difficult within $\langle 1010\rangle$ grains, even though the applied stress continuously increased from the start of the tensile deformation. In compression the basal $\langle a\rangle$ slip is also difficult within $[0001]$ grains due to the inefficient rotation of $[0001]$ grains until C-P2. It is evident that the $[0001]$ and $\langle 1010\rangle$ texture components played an important role in strengthening this alloy.

The LPSO phase could withstand larger loads compared with the $\alpha$-Mg matrix so it prevents the nearby grains from distorting during the tensile and compressive deformation. The LPSO particles aligned with layered interfaces parallel to the ED. It is proposed that the $(0001)$ LPSO is parallel to the layered interface of LPSO phase, and the $(0001)\langle 1120\rangle$ basal slip is the dominant deformation mode at room temperature for the LPSO phase [19,21].A higher stress is needed to deform the LPSO particles along the ED due to the suppression of the basal slip. The LPSO phase reinforces the magnesium matrix to strengthen the alloy via short-fiber strengthening [19]. Additionally, a large number of the bulk $Mg_5$(Gd,Y,Nd) particles distributed along the grain boundaries, these restrict lattice rotation through pinning the grain boundaries in tension and compression. The large volume fraction of $Mg_5$(Gd,Y,Nd) phase improve the strength via dispersion strengthening [30].

# 5 Conclusions

This study investigated the microstructure and texture evolutions during tensile and compressive deformations for a Mg– 11Gd–4.5Y–1Nd–1.5Zn–0.5Zr (wt%) alloy using in-situ synchrotron radiation and subsequent microscopy. The following conclusions were reached:

1. The extruded alloy composed of $\langle 10\bar{1}0\rangle$ fiber texture, $\{1120\}[0001]$ and $\{1120\}\langle 1010\rangle$ texture components. The texture evolves from $[0001]$ to $\langle 1010\rangle$ at T-P3 in tension, but it evolves from $\langle 1010\rangle$ to $[0001]$ at the beginning in compression. The texture evolution is due to a combined contribution of the tensile twinning and non-basal $\langle a\rangle$ slip. The tendency of texture evolution depends on which texture component is favorable for the above deformation modes.

2. The $Mg_5$(Gd,Y,Nd) phase also contributes to the texture development by inducing deformation zone and promoting the nucleation of new grains.

However, the LPSO phase and the $Mg_5$(Gd,Y,Nd) phase retards the texture evolution during the initial deformation stage.

3. The fine recrystallized grains strengthen the alloy. The fine grain size is attributed to the pinning due to bulk $Mg_5$(Gd,Y,Nd) particles at the grain boundaries. The $Mg_5$(Gd,Y,Nd) phase improves the tensile strength via dispersion strengthening. The LPSO phase strengthens the alloy via short-fiber strengthening mechanism. The $[0001]$ and $\langle 1010 \rangle$ textures also contribute to the improvement of strength due to their unfavorable orientations for basal slip.

# Acknowledgments

The authors thank Dr. Jan Bohlen and Dr. Sangbong Yi for their fruitful discussion. Prof. Florian Pyczak and Mr. Uwe Lorenz are acknowledged for the provision of access to the TEM facilities at Helmholtz-Zentrum Geesthacht. The access to the beamline PETRA III at DESY, Hamburg, Germany was provided under the proposal number I-20130153, and the work of N. Schell is greatly appreciated. This work is supported by the National Key Technologies R&D Program (2012BAE01B04, 2012DFH50100, KGFZD-125-13-021, 201001C0104669453). Zijian Yu would like to thank the Chinese Academy of Sciences and German Academic Exchange Service (CAS-DAAD) scholarship program (Grant Number: A/12/ 94735) for the financial support.

# References

1. Y. Kojima, Mater. Trans. 42 (2001) 1154–1159.

2. N. Stanford, M. Barnett, Scr. Mater. 58 (2008) 179–182.

3. T. Homma, N. Kunito, S. Kamado, Scr. Mater. 61 (2009) 644–647.

4. C. Xu, M.Y. Zheng, S.W. Xu, K. Wu, E.D. Wang, S. Kamado, G.J. Wang, X.Y. Lv, Mater. Sci. Eng.: A 547 (2012) 93–98.

5. Z.J. Yu, Y. Huang, X. Qiu, Q. Yang, W. Sun, Z. Tian, D.P. Zhang, J. Meng, Mater. Sci. Eng.: A 578 (2013) 346–353.

6. Z. Yu, Y. Huang, X. Qiu, G. Wang, F. Meng, N. Hort, J. Meng, Mater. Sci. Eng.: A 622 (2015) 121–130.

7. J. Bohlen, S. Yi, D. Letzig, K.U. Kainer, Mater. Sci. Eng.: A 527 (2010) 7092–7098.

8. K. Liu, X. Wang, W. Du, Mater. Sci. Eng.: A 573 (2013) 127–131.

9. J. Bohlen, P. Dobro?, J. Swiostek, D. Letzig, F. Chmelík, P. Luká?, K.U. Kainer, Mater. Sci. Eng.: A 462 (2007) 302–306.

10. Z. Yu, Y. Huang, C.L. Mendis, N. Hort, J. Meng, Mater. Sci. Eng.: A 624 (2015) 23–31.

11. S.R. Agnew, J.A. Horton, T.M. Lillo, D.W. Brown, Scr. Mater. 50 (2004) 377–381.

12. S.R. Agnew, Ö. Duygulu, Int. J. Plast. 21 (2005) 1161–1193.

13. S.B. Yi, H.G. Brokmeier, R.E. Bolmaro, K.U. Kainer, T. Lippmann, Scr. Mater. 51 (2004) 455–460.

14. S.B. Yi, C.H.J. Davies, H.G. Brokmeier, R.E. Bolmaro, K.U. Kainer, J. Homeyer, Acta Mater. 54 (2006) 549–562.

15. A.S. Khan, A. Pandey, T. Gnäupel-Herold, R.K. Mishra, Int. J. Plast. 27 (2011) 688–706.

16. J. Bohlen, M.R. Nürnberg, J.W. Senn, D. Letzig, S.R. Agnew, Acta Mater. 55 (2007) 2101–2112.

17. B. Li, S.P. Joshi, O. Almagri, Q. Ma, K.T. Ramesh, T. Mukai, Acta Mater. 60 (2012) 1818–1826.

18. N. Stanford, R. Cottam, B. Davis, J. Robson, Acta Mater. 78 (2014) 1–13.

19. K. Hagihara, A. Kinoshita, Y. Sugino, M. Yamasaki, Y. Kawamura, H.Y. Yasuda, Y. Umakoshi, Acta Mater. 58 (2010) 6282–6293.

20. K. Hagihara, A. Kinoshita, Y. Fukusumi, M. Yamasaki, Y. Kawamura, Mater. Sci. and Eng.: A 560 (2013) 71–79.

21. K. Hagihara, N. Yokotani, Y. Umakoshi, Intermetallics 18 (2010) 267–276.

22. K. Hagihara, A. Kinoshita, Y. Sugino, M. Yamasaki, Y. Kawamura, H.Y. Yasuda, Y. Umakoshi, Intermetallics 18 (2010) 1079–1085.

23. H.G. Brokmeier, Neutron and Photon Research for Texture and Stress Characterisation of Advanced Materials, in: S. Jiao, Z.Y. Jiang, J.L. Bu (Eds.), Advances in Superalloys, Pts 1 and 2, 2011, pp. 891–894.

24. H.G. Brokmeier, U. Zink, T. Reinert, W. Murach, J. Appl. Crystallogr. 29 (1996) 501–502.

25. J.F. Nie, Metall. Mater. Trans. A 43 (2012) 3891–3939.

26. Y.M. Zhu, A.J. Morton, J.F. Nie, Acta Mater. 60 (2012) 6562–6572.

27. X.H. Shao, Z.Q. Yang, X.L. Ma, Acta Mater. 58 (2010) 4760–4771.

28. M.R. Barnett, Z. Keshavarz, A.G. Beer, D. Atwell, Acta Mater. 52 (2004) 5093–5103.

29. F.J. Humphreys, Acta Metall. 25 (1977) 1323–1344.

30. J.F. Nie, Scr. Mater. 48 (2003) 1009–1015.